Chemical Engineering Journal 428 (2022) 132020

Contents lists available at ScienceDirect

Chemical Engineering Journal

journal homepage: www.elsevier.com/locate/cej

Mechanisms for kerogen wettability transition from water-wet to CO_2-wet: Implications for CO_2 sequestration

Juan Zhou [a,b], Jiajun Zhang [b], Jiapei Yang [c], Zhehui Jin [d], Kai H. Luo [e,*]

[a] Beijing Key Laboratory of CO_2 Capture and Treatment, China Huaneng Clean Energy Research Institute, Beijing 102209, China

[b] Center for Combustion Energy, Key Laboratory for Thermal Science and Power Engineering of Ministry of Education, Department of Energy and Power Engineering, Tsinghua University, Beijing 100084, China

[c] State Key Laboratory of Automotive Safety and Energy, School of Vehicle and Mobility, Tsinghua University, Beijing 100084, China

[d] School of Mining and Petroleum Engineering, Department of Civil and Environmental Engineering, University of Alberta, Edmonton, Alberta T6G 1H9, Canada

[e] Department of Mechanical Engineering, University College London, Torrington Place, London WC1E 7JE, UK

ARTICLE INFO

Keywords:
MD simulation
DFT modelling
CO_2 sequestration
Kerogen wettability

ABSTRACT

Geological CO_2 sequestration (GCS) is an essential building block of the global strategy to alleviate greenhouse gas emissions and mitigate the climate change. Injecting CO_2 into the shale formations can not only reduce carbon emissions but also enhance oil recovery (EOR). Rock wettability is of great importance to CO_2 storage as it determines the efficiency of structural and residual trapping of CO_2 and plays a crucial role in CO_2-EOR. In this work, molecular dynamics (MD) simulations are adopted to investigate the CO_2-H_2O-kerogen systems under various CO_2 pressures. In a vacuum or under low CO_2 pressures, kerogen surface is weakly water-wet thanks to the hydrogen bonding between H_2O and kerogen. As CO_2 pressure increases, kerogen wettability shifts from water-wet to CO_2-wet, because more CO_2 molecules accumulate at the H_2O-kerogen interface and a distinct CO_2 thin film emerges. Density functional theory (DFT) calculations reveal that the O-containing functional groups preferably adsorb H_2O molecules over CO_2 through hydrogen bonding, which is responsible for the weakly water-wet tendency at low CO_2 pressures. In contrast, the carbon skeleton of kerogen exhibits a stronger affinity to CO_2, leading to the formation of CO_2 thin film on the kerogen surface. The CO_2 crowding close to the kerogen surface at high CO_2 pressures gives rise to the CO_2-wet state. This study provides, for the first time, the fundamental mechanism for the kerogen wettability transition from water-wet to CO_2-wet. The work also indicates that wettability of the mature kerogen is more likely to be CO_2-wet during GCS, which is unfavorable for capillary trapping of CO_2, but is favorable for CO_2-EOR.

1. Introduction

Since the Industrial Revolution, the atmospheric CO_2 concentration has been climbing, reaching the level of ~420 ppm as of May 2021, which is ~50% above the pre-industrial level found in 1850 [1]. As a notorious greenhouse gas, excess amount of atmospheric CO_2 can cause global warming. Geological carbon sequestration (GCS) is a promising way to alleviate CO_2 emissions and forms one of the essential building blocks to reach the net-zero carbon emission target [2]. Shale formations have been considered as one of the ideal sites for GCS [3,4]. The geological conditions of shale formations are optimal for CO_2 storage [5] and the highly impermeable clay-bearing caprocks can also effectively seal the sequestrated CO_2 [6]. Furthermore, as GCS is often associated with a high cost, CO_2 enhanced oil recovery (EOR) in shale formations can greatly reduce the financial burden [2].

There are four main geological CO_2 storage mechanisms: structural trapping, where a caprock acts as a seal barrier preventing CO_2 from migrating to shallower zones [7]; residual or capillary trapping, where CO_2 is immobilized by capillary forces in pores and narrow throat in formation rocks [8]; solubility or dissolution trapping, where CO_2 dissolves in the formation water [9]; mineral trapping, where CO_2 reacts with rocks and formation water, forming carbonate minerals [10]. Among these mechanisms, the structural and residual trapping mechanisms are dependent on rock wettability, in which the CO_2-H_2O-rock contact angle plays a crucial role [11]. In the residual trapping, a large amount of free CO_2 gas is trapped by a high capillary force which is strongly dependent on the CO_2-water-rock contact angle, while a water-wet rock is generally favored [12–15].

* Corresponding author.
E-mail address: K.Luo@ucl.ac.uk (K.H. Luo).

https://doi.org/10.1016/j.cej.2021.132020
Received 25 June 2021; Received in revised form 18 August 2021; Accepted 21 August 2021
Available online 26 August 2021

Shale media consist of inorganic and organic matters [16]. The inorganic matters include clay, quartz, and carbonate, and are generally considered hydrophilic [17]. The organic matters mainly consist of kerogen with its content up to 10 wt% [18]. Kerogen contains a considerable number of nano-scale pores with some pore throats size as small as 2 nm or less [19]. Such a narrow pore throat can serve as a prime sealing cap associated with an ultra-high capillary pressure for effective and stable structural and residual trapping. While the conventional wisdom is that kerogen is hydrophobic [20,21], a few recent experimental and simulation studies have shown that kerogen can be weakly water-wet [22–25], which might be attributed to the presence of heteroatoms (O, N, and S) in the kerogen structure [5]. Therefore, understanding about the CO_2-water-kerogen contact angle plays an important role in GCS in shale formations. Besides, the CO_2-water-kerogen contact angle is also closely related to Water alternating gas (WAG) flooding in shale formations [26] for EOR.

The CO_2-water-rock contact angle is dependent on temperature [27–29], pressure [27,30–32], rock type [33], pore structure and connectivity [34–36], and salt concentration [28,37,38], among other factors. Chiquet and coworkers [30] measured CO_2-water-quartz and CO_2-water-mica contact angles under different pressures, and found that as pressure increased from 0 to 11 MPa at 288 K, large increases in the contact angles were observed in the order of 15–25° for quartz and 40–50° for mica. As a result, these two substrates shifted from a water-wet state under a low CO_2 pressure to an intermediate-wet state under a high CO_2 pressure at 288 K. They suggested that the wettability alteration was caused by the pH reduction as well as the increase in CO_2 pressure. Similar phenomena of rock wettability transition were also reported by other experimental studies in the CO_2-water-quartz [31,39] and the CO_2-water-mica [27] systems. Much less attention has been paid to the contact angles of CO_2-water-organic rock systems. Arif et al. [40] measured the contact angles of CO_2-water-coal systems and reported that when the pressure increased from 0.1 MPa to 20 MPa at 323 K, the advancing contact angle increased from 47° to 141° and the receding contact angle increased from 42° to 129°. They explained that the increased contact angle was related to the increased CO_2 adsorption under higher pressure. As for the CO_2-water-kerogen system, Ho et al. [25] reported that the water contact angle on kerogen surface was 42.8° in the absence of CO_2, while the contact angle was 180° when the CO_2 pressure was 200 atm at 300 K, indicating that the kerogen wettability shifted from water-wet to CO_2-wet. They observed that CO_2 formed a thin film on the kerogen surface which might facilitate the wettability change. However, their work focused on CO_2 effects on the water flow in the kerogen nanochannel and paid little attention to the CO_2-induced wettability transition mechanism. While these works reported contact angles in CO_2-water-rock systems over a wide range of pressure, temperature and rock chemistry, there is a lack of direct investigations into the interactions between water and kerogen in the absence/presence of CO_2, and the underlying mechanisms of kerogen wettability transition remain elusive.

A comprehensive understanding of the wettability in CO_2-water-kerogen systems is needed for geological CO_2 sequestration and CO_2-EOR as kerogen is the main constituent of organic matters in shale. In this work, we study interfacial phenomena and evaluate contact angles in CO_2-water-kerogen systems using molecular dynamics (MD) simulations under typical GCS conditions. The contact angle in the CO_2-H_2O-kerogen system increases until reaching 180° as CO_2 pressure increases. The interfacial configurations, density profiles and hydrogen bond densities are carefully analyzed. Moreover, the effect of kerogen heteroatoms on the CO_2-induced contact angle transition is explained by the first-principle density functional theory (DFT) calculations. The work provides a fundamental understanding about CO_2-H_2O-kerogen interactions and reveals the underlying mechanism of wettability variability from sub-atomic and molecular perspectives.

2. Methodology

2.1. Molecular dynamics simulations

The schematic representation of the CO_2-H_2O-kerogen system is shown in Fig. 1. A typical simulation system consists of a cylindrical water droplet residing on the kerogen surface in a CO_2 environment. The simulation box has the dimensions of 110 × 135 × 172 Å^3. The simulation domain is tested to be large enough to eliminate any finite size effect. The cylindrical droplet geometry is employed to avoid the line tension effect [41]. The kerogen surface slab is constructed by MD simulations following the procedures reported in our previous works [42–45]. The Type II-D kerogen molecular model proposed by Ungerer *et al.* [46] is chosen to represent mature kerogens in shale formations. During the simulation, the kerogen structures are modelled using the consistent valence force field (CVFF) [47]. The final size of the kerogen slab is 110 × 135 × 36.5 Å^3. The density of the simulated kerogen is 1.19 g/cm^3, which falls within the range of experimental values of type II kerogen of 1.18–1.35 g/cm^3 [48]. Then, a water droplet consisting of 8,000 H_2O molecules is placed on top of the kerogen surface. Fig. S1 in the Supporting Information (SI) shows the initial configuration of the H_2O-kerogen system in the absence/presence of CO_2. The number of CO_2 molecules in the surrounding CO_2 phase ranges from 0 to 23,300 to represent various pressure conditions ranging from 0 to 60 MPa. The CO_2 density far away from the H_2O droplet and kerogen surface is used to dictate the pressure P by comparing to the NIST Chemistry Webbook [49]. Table 1 summarizes the number of H_2O and CO_2 molecules in the simulation systems. For each case, the values of pressure and the uncertainties were the average value and the standard deviation, respectively, calculated from 5 independent estimates obtained by dividing the 5 ns production run into segments of 1 ns.

Throughout the simulations, the kerogen surface is held stationary, while H_2O and CO_2 molecules can move freely. The H_2O molecules are described by the SPC/E model [50], while we use the rigid TraPPE model to represent the CO_2 molecules [51]. The combination of SPC/E-TraPPE force fields has been proven to be very accurate for describing CO_2-H_2O interaction in the temperature range 323.15–478.15 K and pressures up to 100 MPa [52], in comparison with the experimental data [53]. The Lorentz-Berthelot mixing rules [54] are employed to calculate the interactions between unlike atoms. The non-bonded interactions are represented by the pairwise Coulomb potential and Lennard-Jones (LJ) potential. A cutoff radius of 1 nm is used to compute the LJ interactions with the analytical tail corrections [55]. The long-range electrostatic potential is computed using the PPPM integrations [56]. Periodic boundary conditions are applied in both the x- and y-directions. In the z-direction, a virtual wall is placed at the top of the simulation box which is far away from the H_2O droplet and kerogen surface to confine the CO_2 molecules. The fluid-virtual wall interaction is given by [57,58],

$$u(z) = \begin{cases} \varepsilon_{sf}\left[\frac{2}{15}\left(\frac{\sigma_{sf}}{z}\right)^9 - \left(\frac{\sigma_{sf}}{z}\right)^3\right], z < z_{min} \\ 0, \ z \geqslant z_{min} \end{cases} \quad (1)$$

where z denotes the distance between the fluid molecule and the wall, ε_{sf} and σ_{sf} are obtained from the Lorentz-Berthelot mixing rules of energy and size parameters of CO_2 molecules, respectively. The potential was cut and shifted at its minimum, to ensure that the virtual wall only exerts repulsive force to CO_2 molecules. A vacuum with the same sizes in x- and y-directions and three times of the length of the simulation box in the z-direction is inserted to avoid the artificial influence from the periodic images in the z-direction [55,59]. The entire simulation box including the vacuum space is shown in Fig. S2.

All MD simulations are carried out using the open-source package LAMMPS [60]. The time step is 1 fs. All systems are initially equilibrated for 10 ns in the NVT ensemble and the temperature is maintained at 330

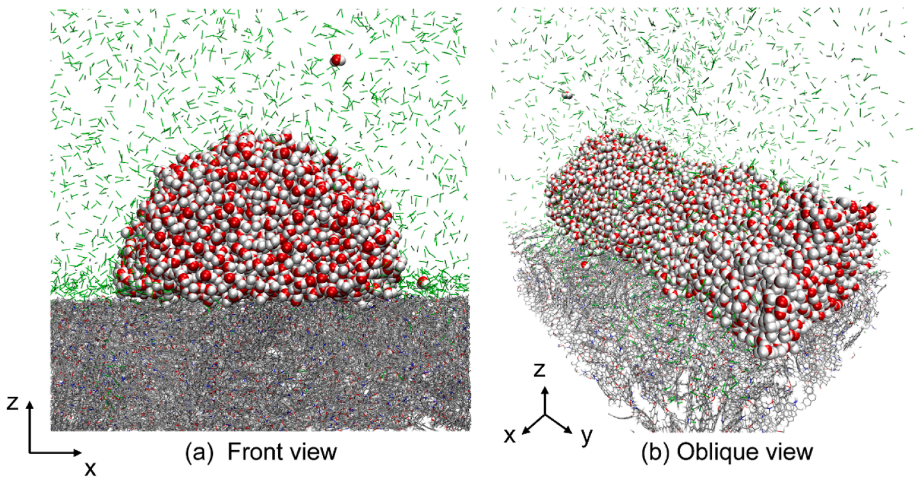

Fig. 1. Schematic representation of a cylindrical water droplet consisting of 8000 H_2O molecules on the kerogen surface in the presence of the CO_2 phase. Within the kerogen matrix, gray, white, red, blue and purple dots represent C, H, O, N and S atoms, respectively. O and H atoms in H_2O molecules are represented by red and white spheres, respectively; CO_2 molecules are represented by green sticks. (For interpretation of the references to color in this figure legend, the reader is referred to the web version of this article.)

Table 1
Simulation settings in CO_2-H_2O-Kerogen systems.

P (MPa)	Number of H_2O molecules	Number of CO_2 molecules
0	8000	0
0.65 ± 0.01	8000	478
4.66 ± 0.04	8000	2962
8.66 ± 0.03	8000	6613
11.24 ± 0.04	8000	10,699
15.95 ± 0.05	8000	16,000
34.26 ± 0.09	8000	20,760
44.42 ± 0.08	8000	22,000
59.36 ± 0.08	8000	23,300

K by using the Nosé–Hoover thermostat [61] with a damping constant of 100 fs. The system is considered to reach equilibrium when little fluctuation can be observed in the density distributions. Then, production runs of 5 ns are conducted and the trajectory snapshots are analyzed to obtain the CO_2-H_2O-kerogen contact angle. Further details regarding the contact angle measurement can be found in the SI.

2.2. DFT calculations

We use DFT to investigate the interactions among CO_2, H_2O and the surface functional groups on kerogen. Competitive adsorption of H_2O and CO_2 on different functional groups are simulated and the role of the main functional groups in the H_2O-CO_2 co-adsorption is studied. The first-principle DFT with dispersion correction of D3 scheme (DFT-D) calculations is implemented in Vienna ab-initio Simulation Package (VASP) [62,63]. All the geometries for modelling are established in MedeA 3.1 from the Materials Design. The projector augmented-wave (PAW) [64] method and the generalized-gradient-approximation (GGA) [65] exchange-correlation functional in the form of Perdew–Burke–Ernzerhof (PBE) [66] are employed in all the calculations. The electronic wave function is expanded on a plane-wave basis with the energy cutoff of 600 eV to converge the relevant quantities. The Brillouin zone is sampled using a 2 × 2 × 1 Monkhorst-Pack k-point with a smearing of 0.1 eV. The self-consistent field (SCF) tolerance is set as 10^{-6} eV/atom. The entire calculation is performed with a convergence threshold of 0.03 eV/Å on the maximum force. No symmetry constraint is used for any modelling. Graphene-based models derived from optimized graphite cell (see Fig. S3) are adopted to simulate the kerogen facets; a 4 × 4 supercell model is used for the graphene and a 6 × 6 supercell model is used for the O-doped graphene, in which the dangling bonds are passivated by H. A 15 Å vacuum region is created above the top of the facets. The adsorption energy is calculated as [67],

$$E_{\text{ads}} = E_{\text{total}} - E_{\text{substrate}} - E_{\text{adsorbate}} \quad (2)$$

where E_{total} is the total energy of the substrate with the adsorbed gas molecule, $E_{\text{substrate}}$ denotes the energy of the bare substrate and $E_{\text{adsorbate}}$ is the energy of the isolated gas molecule. It is widely accepted that the most negative adsorption energy means the most stable configuration.

The energy defined by the following equation is used to evaluate the total interactions of the adsorbates, with the assumption that the variation of adsorption energies over different adsorption sites is negligible.

$$E_{int} = E_{\text{tot}} - E_{CO_2} - E_{H_2O} \quad (3)$$

where E_{tot} is the total co-adsorption energy for the whole system, E_{CO_2} and E_{H_2O} are the total adsorption energies for CO_2 and H_2O, respectively.

3. Results and discussion

In this section, we first calculate the CO_2-H_2O-kerogen contact angle in the absence or presence of CO_2. The effect of CO_2 pressure on the contact angles is analyzed in detail. Then, the underlying mechanisms of kerogen wettability transition induced by the CO_2 pressure increase are discussed via MD and DFT simulations.

3.1. Contact angles on kerogen surface

Two examples of representative equilibrium snapshots and the corresponding two-dimensional (2-D) density contours of water droplets at 0 MPa and 11.24 MPa and 330 K are plotted in Fig. 2a and b. The 2-D density contours of H_2O and CO_2 under the other pressures are given in Fig. S4. When $P \leqslant 4.66$ MPa, the water droplet resides on the kerogen surface and two distinct H_2O adsorption layers are observed on the kerogen surface. The formation of H_2O layering structures can be attributed to the hydrogen bonding between H_2O and kerogen heteroatoms as we will discuss below as well as the entropic effect [68]. As P increases, the two layers become less prominent and the H_2O density distributions close to the kerogen surface become more uniform. At $P =$ 44.40 MPa, the water droplet is completely detached from the kerogen surface. Fig. S4d and f clearly show uniform CO_2 distributions away from the water droplet with its density close to the bulk one. However, in the vicinity of the kerogen surface, significant CO_2 adsorption layers can be observed on both sides of the water droplet. As P increases, the CO_2 density at the H_2O-kerogen interface gradually increases and a distinct CO_2 film emerges at 44.40 MPa, which separates the water droplet from the kerogen surface.

To illustrate the dependence of CO_2-H_2O-kerogen contact angle θ on P, θ versus CO_2 pressure is plotted in Fig. 2c. The kerogen wettability can

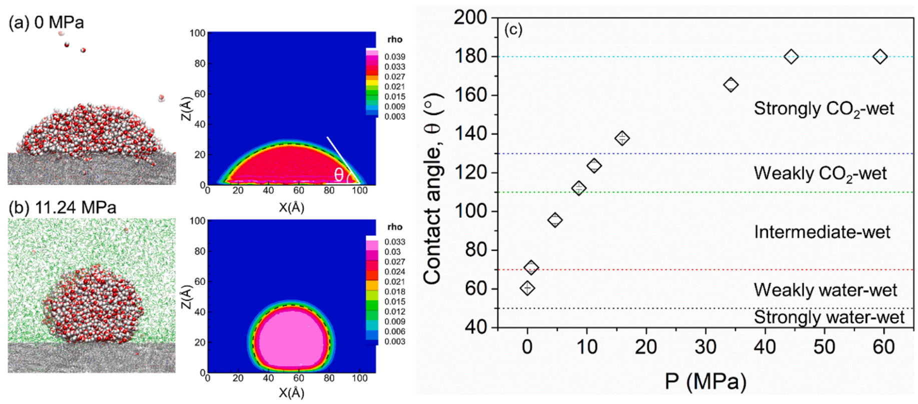

Fig. 2. Water droplet on the kerogen surface at 330 K and at (a) 0 MPa; (b) 11.24 MPa; equilibrium snapshots (left) and 2-D water density contour plots (right). The density is given in the unit of $Å^{-3}$. The dashed lines denote the contour profiles of water: $\rho_w(x,z) = 0.5\rho_b$. (c) CO_2-H_2O-kerogen contact angle as a function of CO_2 pressure.

be classified into five different conditions according to θ based on the definitions given in Ref. [7]. θ shifts from 60.4°±0.2° to 71.0°±1.9° when P increases from 0 MPa to 0.65 MPa. Then, θ reaches 137.9°±0.8° at 15.95 MPa, after which θ continues to increase but with a reduced rate until θ reaches 180° at 44.42 MPa. θ remains at 180° when further increasing P to 59.4 MPa. As P increases, the kerogen wettability shifts from a weakly H_2O-wet state to a strongly CO_2-wet state. Similar trends were observed in CO_2-water–quartz systems [69]. Combined with the analysis on CO_2 density contour plots (Fig. S4d and f), the effect of CO_2 pressure on θ can be attributed to the accumulation of CO_2 molecules at the H_2O-kerogen interfaces.

3.2. Density distributions

H_2O and CO_2 density distributions normal to the kerogen surface as well as the snapshots of the CO_2-H_2O-kerogen systems are displayed in Figs. 3–5. In Fig. 3a, we depict the H_2O and CO_2 density profiles along the center of the water droplet at 4.66 MPa. The density profiles are averaged over a 12 Å-wide strip in the center along the x-direction as illustrated in Fig. 3. The topmost atom of the kerogen slab is defined as the origin in the z-direction. The uneven kerogen surface is responsible for the non-zero density at $z < 0$. Close to the kerogen surface, two prominent H_2O density peaks can be observed at $z = 0.24$ nm and $z = 0.54$ nm with their values at 1.15 and 1.03 g/cm^3, respectively, in line with the layering structures observed in Fig. 2. The H_2O density regresses to its bulk value (0.97 g/cm^3) inside the droplet. On the other hand, CO_2 density profiles render two distinct peaks: one located at the H_2O-kerogen interface; the other one at the H_2O-CO_2 interface. The peak in the vicinity to the kerogen surface indicates the accumulation of CO_2 due to the CO_2-kerogen interactions which are largely hydrophobic interactions. In addition, CO_2 is dissolved within the H_2O droplet. Away from the H_2O droplet, CO_2 density regresses to its bulk value. To better understand the structural properties of the CO_2-H_2O-kerogen system, in Fig. 3b and Fig. 3c, we present the corresponding snapshots showing the entire system and a close-up view of the H_2O-kerogen interface region. They show that a number of CO_2 molecules accumulate at the H_2O-kerogen interface.

Fig. 4(a) Mass density profiles of H_2O and CO_2 averaged over the 12 Å-wide strip normal to the kerogen surface at 15.95 MPa. The snapshot of (b) the entire system; (c) a close-up view of H_2O-kerogen interface region. The color code is the same as Fig. 1.

The thin CO_2 film at the H_2O-kerogen interface continues to grow as CO_2 pressure reaches 34.26 MPa as shown in Fig. 5a. Comparing to Fig. 4a, the peak value in CO_2 density profiles in the vicinity of kerogen surface further increases. As a result, H_2O is depleted from the kerogen surface. The enrichment of CO_2 at the CO_2-H_2O interface disappears at high pressures, in line with previous work [70]. As shown in Fig. 5b, the water droplet is almost completely detached from the kerogen surface and a distinct CO_2 film can be observed. In contrast to Fig. 3c and Fig. 4c, more CO_2 molecules accumulate at the H_2O-kerogen interface.

To reveal the pressure effect on the shape of water droplet, the evolution of droplet contour profiles, defined as the boundary between

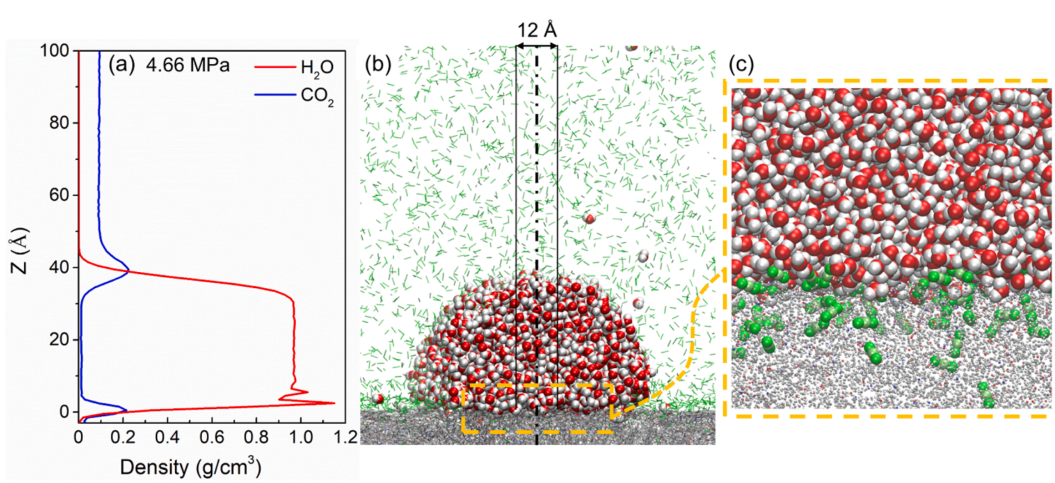

Fig. 3. (a) Mass density profiles of H_2O and CO_2 averaged over the 12 Å-wide strip normal to the kerogen surface at 4.66 MPa. The snapshot of (b) the entire system; (c) a close-up view of H_2O-kerogen interface region. The color code is the same as Fig. 1.

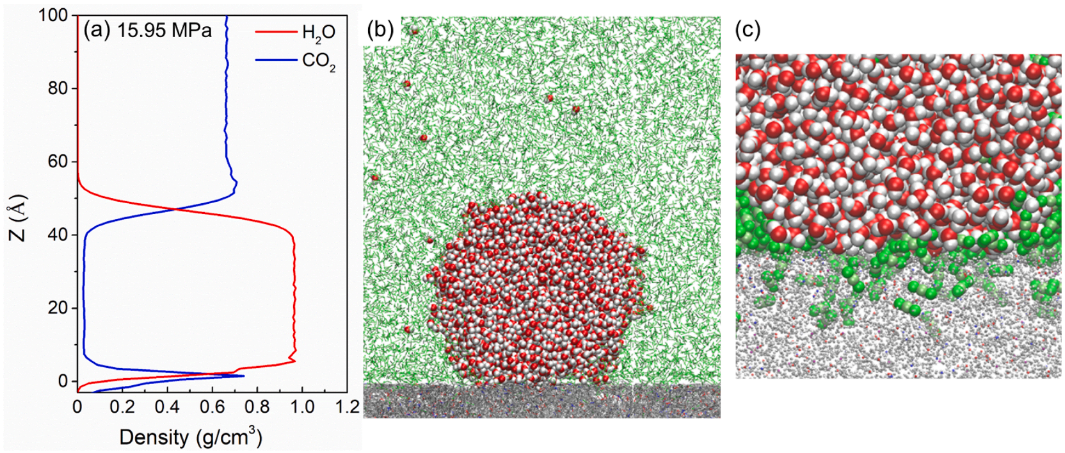

Fig. 4. shows the density profiles of H_2O and CO_2 as well as the corresponding snapshots at 15.95 MPa. In Fig. 4a, a sharp peak at $z = 0.14$ nm is observed in the CO_2 density profile, which highlights the strong accumulation of CO_2 at H_2O-kerogen interfaces, consistent with the finding of Ho et al. [25]. As a result, the H_2O layering structures in the vicinity of kerogen surface become less prominent. This phenomenon can be explained by the snapshots shown in Fig. 4b and c. On the other hand, the enrichment of CO_2 at CO_2-H_2O interface becomes less significant.

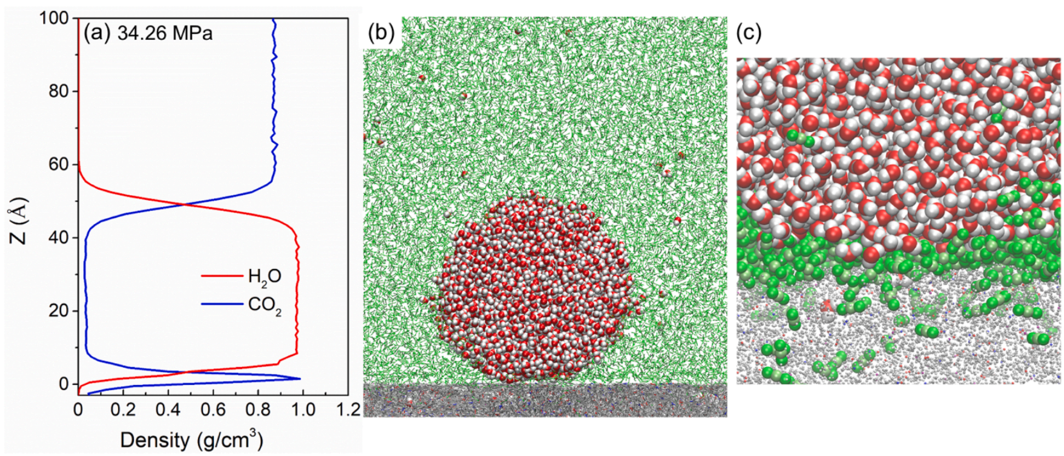

Fig. 5. (a) Mass density profiles of H_2O and CO_2 averaged over the 12 Å-wide strip normal to the kerogen surface at 34.26 MPa. The snapshot of (b) the entire system; (c) a close-up view of H_2O-kerogen interface region. The color code is the same as Fig. 1.

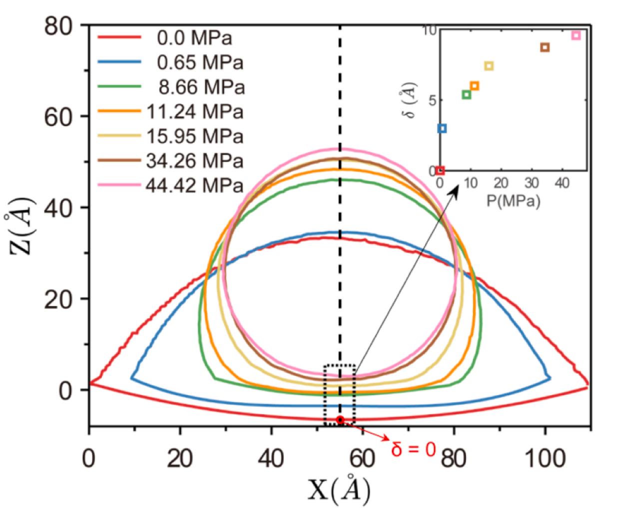

Fig. 6. Water droplet contour profiles as a function of CO_2 pressure. Inset: CO_2 film thickness as a function of CO_2 pressure. The dashed line represents the center of the water droplet.

the droplet and the surrounding where the H_2O mass density equals the CO_2 mass density, is depicted in Fig. 6. It is apparent that as the CO_2 pressure increases, the radius of the water droplet decreases. During this process, the kerogen surface turns from H_2O-wet to CO_2-wet. To quantify the relation between the CO_2 pressure and the CO_2 thin film at the H_2O-kerogen interface, the CO_2 film thickness δ is computed. Due to the roughness of the kerogen surface, it is difficult to distinguish the actual δ. Therefore, we define the intersection of the contour profile and the dashed line in Fig. 6 at 0 MPa as the zero reference ($\delta = 0$). The distance from the intersection to $\delta = 0$ is regarded as an indicator of δ. δ as a function of the CO_2 pressure is displayed in the inset of Fig. 6. The CO_2 film thickness first rapidly increases to 0.30 nm at 0.65 MPa, then the increasing rate slightly declines until 15.95 MPa and the CO_2 film thickness eventually reaches a plateau when the CO_2 pressure further increases to 44.42 MPa. Increase in CO_2 film thickness can be attributed to increasing CO_2 adsorption on kerogen surface with increasing CO_2 pressure. The plateau occurs when a complete adsorption layer is formed. As the water droplet leaves the kerogen surface at a higher pressure indicating a completely CO_2-wet state, we only report the film thickness until 44.42 MPa.

3.3. Hydrogen bond analysis

To further reveal the changes in the water affinity to the kerogen surface with increasing CO_2 pressure, the hydrogen bonds between water and kerogen surface are analyzed. The geometric criterion proposed by Luzar and Chandler [71] is adopted. A hydrogen bond exists if the distance between the donor and acceptor is less than 0.35 nm with the hydrogen-donor–acceptor angle less than 30°. A recent research [72] reported that the strongest interaction between H_2O and kerogen is contributed by hydrogen bonds in which H_2O serves as a donor and the heteroatoms (N, O, and S) in kerogen serve as an acceptor. The N atom shows the highest affinity to H_2O, followed by O and S. In this work, the number of hydrogen bonds between H_2O and the kerogen heteroatoms is calculated and averaged over the 5-ns production runs. As shown in Fig. 7, it is evident that as CO_2 pressure increases, the total number of hydrogen bonds drops gradually. The results demonstrate that the intrusion of CO_2 into the H_2O-kerogen interface greatly diminishes the H_2O-kerogen affinity. In all cases, the O atoms provide the largest fraction of hydrogen bonds (at least 77%), while the S atoms make little contribution. The large hydrogen bond number for O atoms may result from their abundance in kerogen as highlighted in the inset in Fig. 7. The number of O atoms is 2.25 times that of N atoms. The important role of O content in kerogen wettability was also reported by Hu et al. [21]. They found that kerogen wettability may shift from hydrocarbon-wet to water-wet by increasing the number of carbonyl (–C=O) groups on the graphene surface. With the O/C ratio at 20%, the graphene surface with heterogeneously-distributed carbonyl groups is completely water-wet.

3.4. Effect of surface functional groups

H_2O-CO_2 competitive adsorption on kerogen surface is considered to be the key indicator of kerogen wettability. We conduct DFT calculations to reveal the effect of CO_2 on the adsorption of H_2O over the key kerogen surface functional groups. The kerogen model predominantly consists of a carbon skeleton doped with H and O atoms, with a small number of N and S atoms. The carbon skeleton constitutes the main structure of kerogen, while the O functional group plays a dominant role in hydrogen bonding between H_2O and kerogen and their interactions. Herein, graphene and O-doped graphene models are chosen to simulate the representative carbon skeleton and O-containing functional groups on the kerogen surface, respectively. The graphene model is derived from a fully optimized graphite cell and the calculated lattice constants has been validated in Fig. S3. Firstly, we compare the adsorption energy of CO_2 and H_2O molecules on the graphene surface (carbon skeleton of kerogen). The adsorption energy of H_2O on the graphene surface is −0.12 eV, which is consistent with the range of −0.07 eV to −0.13 eV found in previous studies [73–77]. The adsorption energy of CO_2 on graphene surface is −0.15 eV, which is lower than that of H_2O, suggesting that the adsorption of CO_2 on graphene surface is more favorable than H_2O. Then, we investigate the interaction between H_2O and graphene surface (carbon skeleton) in the presence of CO_2. Fig. 8 shows the co-adsorption configurations for H_2O and CO_2 on the graphene surface, and the interaction energy E_{int} as defined in Eq. (3) is listed for each configuration. The E_{int} value of one H_2O molecule on the graphene surface is set at zero as a reference. The E_{int} values for co-adsorption of an H_2O-CO_2 mixture (−0.11 eV) and H_2O-$2CO_2$ mixture (−0.24 eV) on the graphene surface are negative, arising from the interactions among CO_2 and H_2O in both systems. In particular, new hydrogen bonds form between the CO_2 and H_2O molecules. In addition, the presence of CO_2 molecules shifts the H_2O molecule away from the graphene surface. The results imply that H_2O adsorption on the graphene surface is weakened by the presence of CO_2. For further verification, MD simulations are carried out to obtain the contact angles of water droplets on graphene surface under different CO_2 pressures as shown in Fig. S5. Under the same CO_2 pressure, the contact angle on the graphene surface is larger than that on the kerogen surface. The water droplet is completely detached from the graphene surface at 16.32 MPa, while the same phenomenon occurs at 44.42 MPa for the CO_2-H_2O-kerogen system. The results reveal that the aromatic carbon skeleton of kerogen preferably adsorbs CO_2 compared to H_2O, and CO_2 can form a thin film to deplete H_2O molecules from the kerogen surface, in line with our MD simulation results in Section 3.2.

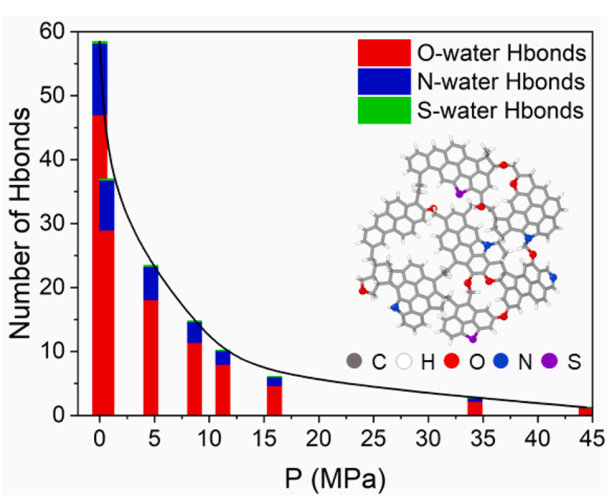

Fig. 7. The number of hydrogen bonds between the kerogen heteroatoms and H_2O as a function of CO_2 pressure at 330 K averaged over the entire 5-ns production. The thin bar at the leftmost side refers to the data at 0 MPa. Inset: The kerogen molecular model.

As discussed in Section 3.3, the O-containing functional groups provide the largest fraction of hydrogen bonds between H_2O and kerogen. Herein, the H_2O-CO_2 competitive adsorption on the O-doped graphene surface is also investigated by DFT simulation to reveal the effect of the O-containing functional groups. According to MD simulations, the epoxy O (Oe) has the highest number of hydrogen bonds among all the O-containing functional groups. The average number of hydrogen bonds per Oe atom is 4.6–5.2 times that of other doped O atoms. Therefore, Oe is chosen to be doped on graphene in the DFT calculation. Firstly, the stable configurations of one H_2O molecule or one CO_2 molecule on the O-doped graphene surface are calculated separately. In the most stable H_2O adsorption configuration, one hydrogen bond is formed between the H_2O molecule and the O-doped graphene surface with a Hw-Oe distance of 0.192 nm, in which Hw represents the H atom in H_2O. Moreover, the adsorption energy of one H_2O molecule (−0.25 eV) on the O-doped graphene surface is much lower than that of CO_2 molecule (−0.18 eV). Then, the adsorption of H_2O on the O-doped graphene surface in the presence of CO_2 is calculated to investigate the role of CO_2 on H_2O adsorption on the O-doped graphene surface. The schematic representations for the H_2O-CO_2 co-adsorption on the O-doped graphene surface are shown in Fig. 9. In the first scenario, two H_2O molecules are located near the doped Oe site, leading to the formation of two hydrogen bonds: one is between the two H_2O molecules; the other is between the H_2O molecule and the doped Oe on the substrate, as shown in Fig. 9a. To illustrate the CO_2 effect, the adsorption of H_2O on the O-doped graphene surface is modelled in the presence of CO_2 molecules, as shown in Fig. 9b and c. The original adsorption positions of the two H_2O molecules in the absence of CO_2 are also displayed in green for comparison. As shown in Fig. 9b, the distance between the H_2O molecules and the substrate only experiences a slight increase. Besides, a small horizontal displacement towards the doped Oe is observed for the H_2O molecule far from the doped Oe, while the other one hardly moves upon the addition of the CO_2 molecule. Such a trend is more obvious in Fig. 9c, in which two CO_2 molecules are placed near the H_2O molecules. The results indicate that the O-containing functional group has a strong interaction with H_2O, which is hardly affected by CO_2. The presence of CO_2 can even push the H_2O molecules closer to the functional group.

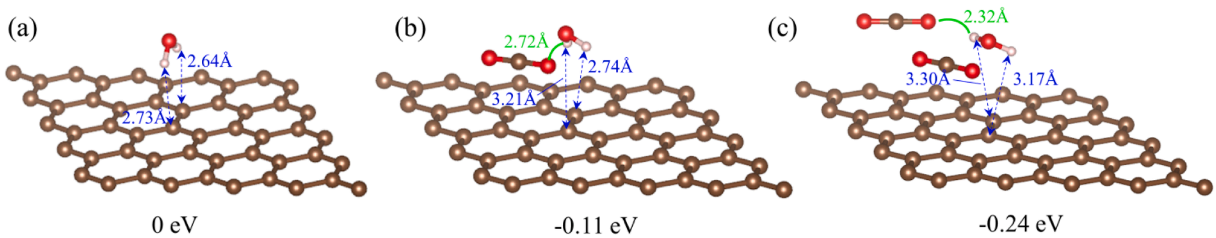

Fig. 8. Optimized structures for one H_2O molecule adsorbed on graphene surface in the presence of (a) zero CO_2 molecule; (b) one CO_2 molecule; (c) two CO_2 molecules. The red, white and brown spheres represent O, H and C, respectively. (For interpretation of the references to color in this figure legend, the reader is referred to the web version of this article.)

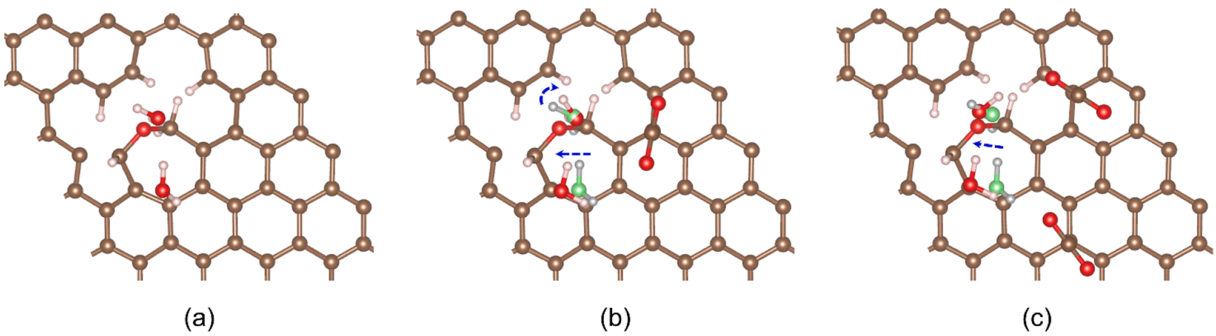

Fig. 9. Top views of optimized structures for two H_2O molecules adsorbed onto O-doped graphene surface in the presence of (a) zero CO_2 molecule; (b) one CO_2 molecule; (c) two CO_2 molecules. The red, white, brown spheres represent O, H and C, respectively. The green spheres represent the original positions of O atoms in H_2O before the CO_2 addition. Displacements of the H_2O molecules are highlighted by the blue arrows. (For interpretation of the references to color in this figure legend, the reader is referred to the web version of this article.)

While this result is seemingly in a stark contrast to the role of CO_2 pressure on CO_2-H_2O-kerogen contact angle as discussed above, we note that the DFT simulations are conducted at the conditions in which there are a very small number of CO_2 molecules. It rather endorses the formation of hydrogen bonding between H_2O and kerogen surface, and explains why kerogen still behaves as a weakly water-wet [22–25] or intermediate-wet substrate at a relatively low CO_2 pressure as shown in Fig. 2. On the other hand, as CO_2 pressure further increases, due to the strong interactions between CO_2 and carbon skeleton as shown in Fig. 8, more CO_2 molecules accumulate in the vicinity of kerogen surface. The formation and constant-growth of CO_2 thin film would influence the formation of hydrogen bonding between H_2O and kerogen surface. This phenomenon can be attributed to the correlation effect among CO_2, H_2O and kerogen which can be fully captured by MD simulations. On the other hand, DFT simulations cannot grasp such effect due to high computational costs. The correlation effect stems from intermolecular interactions and molecular configurations and is important when a large number of fluid molecules gather at the interface [78]. For example, a specific fluid molecule distribution close to the substrate is dependent not only on fluid-surface interactions but also molecular configurations of the surrounding fluid. In other words, in a vacuum or at a low CO_2 pressure, the CO_2-H_2O-kerogen contact angle is mainly determined by H_2O-kerogen and H_2O-H_2O interactions which can be revealed from DFT as well as MD simulations, while it is greatly affected by CO_2 crowding driven by the hydrophobic interactions at a high CO_2 pressure which can only be captured by MD simulations. For further verification, supplementary MD simulations are carried out to calculate the contact angles of water droplets on graphene and O-doped graphene surface (Oe doped) under different CO_2 pressures. The results are provided in Fig. S5. Under the same CO_2 pressure, the water contact angle on the graphene surface is larger than that on the O-doped graphene surface, and the H_2O droplet is totally detached from the graphene surface at 16.32 MPa, while the same phenomenon occurs at 18.77 MPa for the O-doped graphene system. Besides, as shown in Fig. S5c, the density of the CO_2 adsorption layer near the graphene surface is larger than that of the O-doped graphene surface under 8.85 MPa. These results further verify the CO_2 pressure effects and reveal that CO_2 can potentially form a thin film with increasing pressure and repel H_2O molecules from the kerogen surface.

4. Conclusions

In this work, the effect of CO_2 pressure on the CO_2-H_2O-kerogen contact angle is investigated through MD and DFT simulations. The simulation results show that the contact angle increases from 60.4° to 180° when the CO_2 pressure increases from 0 to 44.42 MPa. The presence of CO_2 results in a gradual transition in the kerogen wettability from H_2O-wet to CO_2-wet. At low CO_2 pressures, CO_2 and H_2O co-adsorb at the solid–fluid interface. As CO_2 pressure increases, a distinct CO_2 film is observed at the H_2O-kerogen interface, leading to a sharp decline in the number of hydrogen bonds between H_2O and kerogen. The H_2O-kerogen interaction is dominated by the hydrogen bonding, while the O-containing functional groups on the kerogen surface contribute the majority of hydrogen bonds. According to the DFT calculations, the presence of CO_2 pushes the H_2O molecule closer to the Oe group on the O-doped graphene substrate. However, on the graphene surface, CO_2 has a lower adsorption energy than H_2O, while CO_2 can push H_2O away from the substrate. Therefore, in a vacuum or at a low CO_2 pressure, the CO_2-H_2O-kerogen contact angle is mainly determined by H_2O-kerogen and H_2O-H_2O interactions, while it is greatly affected by CO_2 crowding driven by the hydrophobic interactions at a high CO_2 pressure. Our work indicates that the highly-matured kerogen with a relatively low O content is prone to wettability change in the presence of CO_2. The CO_2-wet state at high pressures is unfavorable for CO_2 residual trapping, but is favorable for the water alternating gas process for EOR.

Declaration of Competing Interest

The authors declare that they have no known competing financial interests or personal relationships that could have appeared to influence the work reported in this paper.

Acknowledgements

Support from the MOST National Key Research and Development Programme (Project No. 2016YFB0600805) and the Center for Combustion Energy at Tsinghua University is gratefully acknowledged. The simulations were partly performed on the High-Performance Parallel Computer supported by the Tsinghua HPC Platform. Additional support from the UK Engineering and Physical Sciences Research Council under the project UK Consortium on Mesoscale Engineering Sciences (UKCOMES) (Grant No. EP/R029598/1) is gratefully acknowledged. China Huaneng Group science and technology project (HNKJ21-H51) is acknowledged. Z. J. acknowledges a Discovery Grant from Natural Sciences and Engineering Research Council of Canada (NSERC RGPIN-2017-05080).

Appendix A. Supplementary data

Supplementary data to this article can be found online at https://doi.org/10.1016/j.cej.2021.132020.

References

[1] P. Tans, R. Keeling, NOAA, Atmospheric CO2 Level Monthly, Measurement (2021) www.esrl.noaa.gov/gmd/ccgg/trends/.

[2] M. Bui, C.S. Adjiman, A. Bardow, E.J. Anthony, A. Boston, S. Brown, P.S. Fennell, S. Fuss, A. Galindo, L.A. Hackett, J.P. Hallett, H.J. Herzog, G. Jackson, J. Kemper, S. Krevor, G.C. Maitland, M. Matuszewski, I.S. Metcalfe, C. Petit, G. Puxty, J. Reimer, D.M. Reiner, E.S. Rubin, S.A. Scott, N. Shah, B. Smit, J.P.M. Trusler, P. Webley, J. Wilcox, N. Mac Dowell, Carbon capture and storage (CCS): The way forward, Energy Environ. Sci. 11 (5) (2018) 1062–1176, https://doi.org/10.1039/C7EE02342A.

[3] Y. Liu, P. Wang, M. Yang, Y. Zhao, J. Zhao, Y. Song, CO2 sequestration in depleted methane hydrate sandy reservoirs, J. Nat. Gas Sci. Eng. 49 (2018) 428–434, https://doi.org/10.1016/j.jngse.2017.10.023.

[4] M.D. Aminu, S.A. Nabavi, C.A. Rochelle, V. Manovic, A review of developments in carbon dioxide storage, Appl. Energy 208 (2017) 1389–1419, https://doi.org/10.1016/j.apenergy.2017.09.015.

[5] W. Li, M. Zhang, Y. Nan, W. Pang, Z. Jin, Molecular dynamics study on CO2 storage in water-filled kerogen nanopores in shale reservoirs: Effects of kerogen maturity and pore size, Langmuir 37 (1) (2021) 542–552, https://doi.org/10.1021/acs.langmuir.0c0323210.1021/acs.langmuir.0c03232.s001.

[6] G. Rother, E.S. Ilton, D. Wallacher, T. Hauβ, H.T. Schaef, O. Qafoku, K.M. Rosso, A. R. Felmy, E.G. Krukowski, A.G. Stack, N. Grimm, R.J. Bodnar, CO2 sorption to subsingle hydration layer montmorillonite clay studied by excess sorption and neutron diffraction measurements, Environ. Sci. Technol. 47 (1) (2013) 205–211, https://doi.org/10.1021/es301382y.

[7] S. Iglauer, C.H. Pentland, A. Busch, CO2 wettability of seal and reservoir rocks and the implications for carbon geo-sequestration, Water Resour. Res. 51 (1) (2015) 729–774, https://doi.org/10.1002/2014WR015553.

[8] M.A. Hesse, F.M. Orr, H.A. Tchelepi, Gravity currents with residual trapping, J. Fluid Mech. 611 (2008) 35–60, https://doi.org/10.1017/S002211200800219X.

[9] E. Lindeberg, D. Wessel-Berg, Vertical convection in an aquifer column under a gas cap of CO2, Energy Convers. Manage. 38 (1997) 229–234, https://doi.org/10.1016/s0196-8904(96)00274-9.

[10] I. Gaus, Role and impact of CO2-rock interactions during CO2 storage in sedimentary rocks, Int. J. Green. Gas Control 4 (1) (2010) 73–89, https://doi.org/10.1016/j.ijggc.2009.09.015.

[11] S. Iglauer, CO2-Water-Rock Wettability: Variability, Influencing Factors, and Implications for CO2 Geostorage, Acc. Chem. Res. 50 (5) (2017) 1134–1142, https://doi.org/10.1021/acs.accounts.6b00602.

[12] S. Iglauer, A.Z. Al-yaseri, R. Rezaee, M. Lebedev, CO2 wettability of caprocks: Implications for structural storage capacity and containment security, Geophys. Res. Lett. 42 (2015) 9279–9284, https://doi.org/10.1002/2015GL065787.Received.

[13] K. Chaudhary, M. Bayani Cardenas, W.W. Wolfe, J.A. Maisano, R.A. Ketcham, P. C. Bennett, Pore-scale trapping of supercritical CO2 and the role of grain wettability and shape, Geophys. Res. Lett. 40 (15) (2013) 3878–3882, https://doi.org/10.1002/grl.50658.

[14] T. Rahman, M. Lebedev, A. Barifcani, S. Iglauer, Residual trapping of supercritical CO2 in oil-wet sandstone, J. Colloid Interface Sci. 469 (2016) 63–68, https://doi.org/10.1016/j.jcis.2016.02.020.

[15] A.S. Al-Menhali, H.P. Menke, M.J. Blunt, S.C. Krevor, Pore scale observations of trapped co2 in mixed-wet carbonate rock: applications to storage in oil fields, Environ. Sci. Technol. 50 (18) (2016) 10282–10290, https://doi.org/10.1021/acs.est.6b0311110.1021/acs.est.6b03111.s001.

[16] K. McCarthy, K. Rojas, M. Niemann, D. Palmowski, K. Peters, A. Stankiewicz, Basic petroleum geochemistry for source rock evaluation, Oilfield Review. 23 (2011) 32–43, https://doi.org/10.1016/j.epsl.2006.01.027.

[17] D.J.K. Ross, R. Marc Bustin, The importance of shale composition and pore structure upon gas storage potential of shale gas reservoirs, Mar. Pet. Geol. 26 (6) (2009) 916–927, https://doi.org/10.1016/j.marpetgeo.2008.06.004.

[18] Y. Shi, M.R. Yassin, L. Yuan, H. Dehghanpour, Modelling imbibition data for determining size distribution of organic and inorganic pores in unconventional rocks, Int. J. Coal Geol. 201 (2019) 26–43, https://doi.org/10.1016/j.coal.2018.11.010.

[19] G.R. Chalmers, R.M. Bustin, I.M. Power, Characterization of gas shale pore systems by porosimetry, pycnometry, surface area, and field emission scanning electron microscopy/transmission electron microscopy image analyses: examples from the barnett woodford, haynesville, marcellus, and doig uni, AAPG Bulletin. 96 (2012) 1099–1119, https://doi.org/10.1306/10171111052.

[20] A. Jagadisan, Z. Heidari, Experimental quantification of the effect of thermal maturity of kerogen on its wettability, SPE Reservoir Eval. Eng. 22 (2019) 1323–1333, https://doi.org/10.2118/195684-PA.

[21] Y. Hu, D. Devegowda, R. Sigal, A microscopic characterization of wettability in shale kerogen with varying maturity levels, J. Nat. Gas Sci. Eng. 33 (2016) 1078–1086, https://doi.org/10.1016/j.jngse.2016.06.014.

[22] M.R. Yassin, M. Begum, H. Dehghanpour, Organic shale wettability and its relationship to other petrophysical properties: A Duvernay case study, Int. J. Coal Geol. 169 (2017) 74–91, https://doi.org/10.1016/j.coal.2016.11.015.

[23] A. Jagadisan, Z. Heidari, Impacts of competitive water adsorption of kerogen and clay minerals on wettability of organic-rich mudrocks, SPE Reservoir Eval. Eng. 23 (2020) 1180–1189, https://doi.org/10.2118/201202-PA.

[24] L. Liang, D. Luo, X. Liu, J. Xiong, Experimental study on the wettability and adsorption characteristics of Longmaxi Formation shale in the Sichuan Basin China, J. Nat. Gas Sci. Eng. 33 (2016) 1107–1118, https://doi.org/10.1016/j.jngse.2016.05.024.

[25] T.A. Ho, Y. Wang, A. Ilgen, L.J. Criscenti, C.M. Tenney, Supercritical CO2-induced atomistic lubrication for water flow in a rough hydrophilic nanochannel, Nanoscale. 10 (42) (2018) 19957–19963, https://doi.org/10.1039/C8NR06204H.

[26] L. Han, Y. Gu, Optimization of miscible CO2 water-alternating-gas injection in the bakken formation, Energy Fuels 28 (11) (2014) 6811–6819, https://doi.org/10.1021/ef501547x.

[27] M. Arif, A.Z. Al-Yaseri, A. Barifcani, M. Lebedev, S. Iglauer, Impact of pressure and temperature on CO2-brine-mica contact angles and CO2-brine interfacial tension: Implications for carbon geo-sequestration, J. Colloid Inter. Sci. 462 (2016) 208–215, https://doi.org/10.1016/j.jcis.2015.09.076.

[28] M. Arif, A. Barifcani, M. Lebedev, S. Iglauer, Structural trapping capacity of oil-wet caprock as a function of pressure, temperature and salinity, Int. J. Greenhouse Gas Control 50 (2016) 112–120, https://doi.org/10.1016/j.ijggc.2016.04.024.

[29] D. Broseta, N. Tonnet, V. Shah, Are rocks still water-wet in the presence of dense CO2 or H2S? Geofluids. 12 (2012) 280–294, https://doi.org/10.1111/j.1468-8123.2012.00369.x.

[30] P. Chiquet, D. Broseta, S. Thibeau, Wettability alteration of caprock minerals by carbon dioxide, Geofluids. 7 (2) (2007) 112–122, https://doi.org/10.1111/gfl.2007.7.issue-210.1111/j.1468-8123.2007.00168.x.

[31] J.-W. Jung, J. Wan, Supercritical CO2 and ionic strength effects on wettability of silica surfaces: Equilibrium contact angle measurements, Energy Fuels 26 (9) (2012) 6053–6059, https://doi.org/10.1021/ef300913t.

[32] P.K. Bikkina, Contact angle measurements of CO2-water-quartz/calcite systems in the perspective of carbon sequestration, Int. J. Greenhouse Gas Control 5 (5) (2011) 1259–1271, https://doi.org/10.1016/j.ijggc.2011.07.001.

[33] C.A. Fauziah, A.Z. Al-Yaseri, N.K. Jha, C. Lagat, H. Roshan, A. Barifcani, S. Iglauer, Carbon dioxide wettability of south west hub sandstone, western australia: implications for carbon geo-storage, Int. J. Greenhouse Gas Control 98 (2020) 103064, https://doi.org/10.1016/j.ijggc.2020.103064.

[34] E. Ghanbari, H. Dehghanpour, Impact of rock fabric on water imbibition and salt diffusion in gas shales, Int. J. Coal Geol. 138 (2015) 55–67, https://doi.org/10.1016/j.coal.2014.11.003.

[35] Q. Lan, M. Xu, M. Binazadeh, H. Dehghanpour, J.M. Wood, A comparative investigation of shale wettability: The significance of pore connectivity, J. Nat. Gas Sci. Eng. 27 (2015) 1174–1188, https://doi.org/10.1016/j.jngse.2015.09.064.

[36] M.G. Kibria, Q. Hu, H. Liu, Y. Zhang, J. Kang, Pore structure, wettability, and spontaneous imbibition of Woodford Shale permian basin, west texas, Marine Petrol. Geol. 91 (2018) 735–748, https://doi.org/10.1016/j.marpetgeo.2018.02.001.

[37] A.Z. Al-Yaseri, H. Roshan, M. Lebedev, A. Barifcani, S. Iglauer, Dependence of quartz wettability on fluid density, Geophys. Res. Lett. 43 (8) (2016) 3771–3776, https://doi.org/10.1002/2016GL068278.

[38] D.N. Espinoza, J.C. Santamarina, Water-CO2-mineral systems: Interfacial tension, contact angle, and diffusion-Implications to CO2 geological storage, Water Resour. Res. 46 (2010) 1–10, https://doi.org/10.1029/2009WR008634.

[39] F. Alnili, A. Al-Yaseri, H. Roshan, T. Rahman, M. Verall, M. Lebedev, M. Sarmadivaleh, S. Iglauer, A. Barifcani, Carbon dioxide/brine wettability of porous sandstone versus solid quartz: An experimental and theoretical investigation, J. Colloid Interface Sci. 524 (2018) 188–194, https://doi.org/10.1016/j.jcis.2018.04.029.

[40] M. Arif, A. Barifcani, M. Lebedev, S. Iglauer, CO2-wettability of low to high rank coal seams: Implications for carbon sequestration and enhanced methane recovery, Fuel 181 (2016) 680–689, https://doi.org/10.1016/j.fuel.2016.05.053.
[41] G. Scocchi, D. Sergi, C. D'Angelo, A. Ortona, Wetting and contact-line effects for spherical and cylindrical droplets on graphene layers: A comparative molecular-dynamics investigation, Phys. Review E – Statis. Nonlin. Soft Matter Phys. 84 (2011) 1–8, https://doi.org/10.1103/PhysRevE.84.061602.
[42] J. Zhou, Q. Mao, K.H. Luo, Effects of moisture and salinity on methane adsorption in kerogen: a molecular simulation study, Energy Fuels 33 (6) (2019) 5368–5376, https://doi.org/10.1021/acs.energyfuels.9b0039210.1021/acs.energyfuels.9b00392.s001.
[43] J. Zhou, Z. Jin, K.H. Luo, Effects of Moisture Contents on Shale Gas Recovery and CO2 Sequestration, Langmuir 35 (26) (2019) 8716–8725, https://doi.org/10.1021/acs.langmuir.9b00862.
[44] J. Zhou, Z. Jin, K.H. Luo, Insights into recovery of multi-component shale gas by CO2 injection: A molecular perspective, Fuel 267 (2020) 117247, https://doi.org/10.1016/j.fuel.2020.117247.
[45] J. Zhou, Z. Jin, K.H. Luo, The role of brine in gas adsorption and dissolution in kerogen nanopores for enhanced gas recovery and CO2 sequestration, Chem. Eng. J. 399 (2020) 125704, https://doi.org/10.1016/j.cej.2020.125704.
[46] P. Ungerer, J. Collell, M. Yiannourakou, Molecular modeling of the volumetric and thermodynamic properties of kerogen: Influence of organic type and maturity, Energy Fuels 29 (1) (2015) 91–105, https://doi.org/10.1021/ef502154k.
[47] P. Dauber-Osguthorpe, V.A. Roberts, D.J. Osguthorpe, J. Wolff, M. Genest, A. T. Hagler, Structure and energetics of ligand binding to proteins: Escherichia coli dihydrofolate reductase???trimethoprim, a drug???receptor system Proteins: Structure, Fun. Bioinformatics. 4 (1) (1988) 31–47, https://doi.org/10.1002/(ISSN)1097-013410.1002/prot.v4:110.1002/prot.340040106.
[48] K.S. Okiongbo, A.C. Aplin, S.R. Larter, Changes in type ii kerogen density as a function of maturity: evidence from the kimmeridge, Clay Formation (2005), https://doi.org/10.1021/ef050194.
[49] E. Lemmon, M. McLinden, M. Huber, NIST reference fluid thermodynamic and transport properties—REFPROP, (n.d.).
[50] H.J.C. Berendsen, J.R. Grigera, T.P. Straatsma, The missing term in effective pair potentials, J. Phys. Chem. 91 (24) (1987) 6269–6271, https://doi.org/10.1021/j100308a038.
[51] J.J. Potoff, J.I. Siepmann, Vapor-liquid equilibria of mixtures containing alkanes, carbon dioxide, and nitrogen, AIChE Journal. 47 (7) (2001) 1676–1682, https://doi.org/10.1002/(ISSN)1547-590510.1002/aic.v47:710.1002/aic.690470719.
[52] O.A. Moultos, I.N. Tsimpanogiannis, A.Z. Panagiotopoulos, I.G. Economou, Atomistic molecular dynamics simulations of CO2 diffusivity in H2O for a wide range of temperatures and pressures, J. Phys. Chem. B 118 (20) (2014) 5532–5541, https://doi.org/10.1021/jp502380r.
[53] S.P. Cadogan, G.C. Maitland, J.P.M. Trusler, Diffusion coefficients of CO2 and N2 in water at temperatures between 298.15 K and 423.15 K at pressures up to 45 MPa, J. Chem. Eng. Data 59 (2) (2014) 519–525, https://doi.org/10.1021/je401008s.
[54] H.A. Lorentz, Ueber die Anwendung des Satzes vom Virial in der kinetischen Theorie der Gase, Annalen Der Physik. 248 (1) (1881) 127–136, https://doi.org/10.1002/(ISSN)1521-388910.1002/andp.v248:110.1002/andp.18812480110.
[55] D. Frenkel, B. Smit, Understanding Molecular Simulation, From Algorithms to App. (2002).
[56] W.M. Brown, A. Kohlmeyer, S.J. Plimpton, A.N. Tharrington, Implementing molecular dynamics on hybrid high performance computers - Particle-particle particle-mesh, Comput. Phys. Commun. 183 (3) (2012) 449–459, https://doi.org/10.1016/j.cpc.2011.10.012.
[57] M. Lupkowski, F. van Swol, Computer simulation of fluids interacting with fluctuating walls, J. Chem. Phys. 93 (1) (1990) 737–745, https://doi.org/10.1063/1.459524.
[58] Z. Jin, Effect of nano-confinement on high pressure methane flow characteristics, J. Nat. Gas Sci. Eng. 45 (2017) 575–583, https://doi.org/10.1016/j.jngse.2017.06.007.
[59] J.C. Shelley, G.N. Patey, Boundary condition effects in simulations of water confined between planar walls, Mol. Phys. 88 (1996) 385–398, https://doi.org/10.1080/00268979650026406.
[60] S. Plimpton, Fast parallel algorithms for short-range molecular-dynamics, J. Comput. Phys. 117 (1) (1995) 1–19, https://doi.org/10.1006/jcph.1995.1039.
[61] W.G. Hoover, Canonical dynamics: Equilibrium phase-space distributions, Phys. Rev. A 31 (1985) 1695–1697, https://doi.org/10.3390/ph9020024.
[62] G. Kresse, J. Furthmüller, Efficiency of ab-initio total energy calculations for metals and semiconductors using a plane-wave basis set, Comput. Mater. Sci. 6 (1) (1996) 15–50, https://doi.org/10.1016/0927-0256(96)00008-0.
[63] G. Kresse, J. Hafner, Ab initio molecular dynamics for open-shell transition metals, Physical Review B. 48 (17) (1993) 13115–13118, https://doi.org/10.1103/PhysRevB.48.13115.
[64] J.C. Sancho-García, J.L. Brédas, J. Cornil, Assessment of the reliability of the Perdew–Burke–Ernzerhof functionals in the determination of torsional potentials in π-conjugated molecules, Chem. Phys. Lett. 377 (1-2) (2003) 63–68, https://doi.org/10.1016/S0009-2614(03)01086-8.
[65] J.P. Perdew, K. Burke, M. Ernzerhof, Generalized gradient approximation made simple, Phys. Rev. Lett. 77 (18) (1996) 3865–3868, https://doi.org/10.1103/PhysRevLett.77.3865.
[66] S. Grimme, Semiempirical GGA-type density functional constructed with a long-range dispersion correction, J. Comput. Chem. 27 (15) (2006) 1787–1799, https://doi.org/10.1002/(ISSN)1096-987X10.1002/jcc.v27:1510.1002/jcc.20495.
[67] A. Abbasi, J.J. Sardroodi, Exploration of sensing of nitrogen dioxide and ozone molecules using novel TiO 2 /Stanene heterostructures employing DFT calculations, Appl. Surf. Sci. 442 (2018) 368–381, https://doi.org/10.1016/j.apsusc.2018.02.183.
[68] J. Wu, T. Jiang, D.E. Jiang, Z. Jin, D. Henderson, A classical density functional theory for interfacial layering of ionic liquids, Soft Matter 7 (2011) 11222–11231, https://doi.org/10.1039/c1sm06089a.
[69] S. Iglauer, M.S. Mathew, F. Bresme, Molecular dynamics computations of brine-CO2 interfacial tensions and brine-CO2-quartz contact angles and their effects on structural and residual trapping mechanisms in carbon geo-sequestration, J. Colloid Interface Sci. 386 (1) (2012) 405–414, https://doi.org/10.1016/j.jcis.2012.06.052.
[70] H. Monhemi, S. Dolatabadi, Molecular dynamics simulation of high-pressure CO2 pasteurization reveals the interfacial denaturation of proteins at CO2/water interface, J. CO2 Util. 35 (2020) 256–264, https://doi.org/10.1016/j.jcou.2019.10.004.
[71] A. Luzar, D. Chandler, Structure and hydrogen bond dynamics of water-dimethyl sulfoxide mixtures by computer simulations, J. Chem. Phys. 98 (10) (1993) 8160–8173, https://doi.org/10.1063/1.464521.
[72] L.O. Lawal, T. Olayiwola, S. Abdel-Azeim, M. Mahmoud, A.O. Onawole, M. S. Kamal, Molecular simulation of kerogen-water interaction: Theoretical insights into maturity, J. Mol. Liq. 299 (2020) 112224, https://doi.org/10.1016/j.molliq.2019.112224.
[73] J. Ma, A. Michaelides, D. Alfè, L. Schimka, G. Kresse, E. Wang, Adsorption and diffusion of water on graphene from first principles, Phys. Review B – Conden. Matter Mater. Phys. 84 (3) (2011), https://doi.org/10.1103/PhysRevB.84.033402.
[74] M. Rubeš, P. Nachtigall, J. Vondrášek, O. Bludský, Structure and stability of the water-graphite complexes, J. Phys. Chem. C 113 (19) (2009) 8412–8419, https://doi.org/10.1021/jp901410m.
[75] E. Voloshina, D. Usvyat, M. Schütz, Y. Dedkov, B. Paulus, On the physisorption of water on graphene: A CCSD(T) study, PCCP 13 (2011) 12041–12047, https://doi.org/10.1039/c1cp20609e.
[76] D. Feller, K.D. Jordan, Estimating the strength of the water/single-layer graphite interaction, J. Phys. Chem. A 104 (44) (2000) 9971–9975, https://doi.org/10.1021/jp001766o.
[77] G.R. Jenness, O. Karalti, K.D. Jordan, Benchmark calculations of water–acene interaction energies: Extrapolation to the water–graphene limit and assessment of dispersion–corrected DFT methods, PCCP 12 (2010) 6375–6381, https://doi.org/10.1039/c000988a.
[78] Z. Jin, Y. Tang, J. Wu, A perturbative density functional theory for square-well fluids, J. Chem. Phys. 134 (17) (2011) 174702, https://doi.org/10.1063/1.3585677.